

# Crack to pulse transition and magnitude statistics during earthquake cycles on a self-similar rough fault

Elías Rafn Heimisson<sup>a,\*</sup>

<sup>a</sup>*Seismological Laboratory, California Institute of Technology, Pasadena, California, USA*

---

## Abstract

Faults in nature demonstrate fluctuations from planarity at most length scales that are relevant for earthquake dynamics. These fluctuations may influence all stages of the seismic cycle; earthquake nucleation, propagation, arrest, and inter-seismic behavior. Here I show quasi-dynamic plane-strain simulations of earthquake cycles on a self-similar 10 km long rough fault with amplitude-to-wavelength ratio  $\alpha = 0.01$ . The minimum roughness wavelength,  $\lambda_{min}$ , and nucleation length scales are well resolved and much smaller than the fault length. Stress dissipation and fault loading is implemented using a variation of the backslip approach, which allows for efficient simulations of multiple cycles without stresses becoming unrealistically large. I explore varying  $\lambda_{min}$  for the same stochastically generated realization of a rough fractal fault. Decreasing  $\lambda_{min}$  causes the minimum and maximum earthquake sizes to decrease. Thus the fault seismicity is characterized by smaller and more numerous earthquakes, on the other hand, increasing the  $\lambda_{min}$  results in fewer and larger events. However, in all cases, the inferred b-value is constant and the same as for a reference no-roughness simulation ( $\alpha = 0$ ). Further, the characteristics of individual ruptures are also altered and here I highlight a new mechanism for generating pulse-like ruptures. Seismic events are initially crack-like, but at a critical length scale, they continue to propagate as pulses, locking in an approximately fixed amount of slip. I investigate this transition using simple arguments and derive a characteristic pulse length and slip distance based on roughness drag. I hypothesize that the ratio  $\lambda_{min}/\alpha^2$  could be roughly estimated from kinematic rupture models. Furthermore, I suggest that the ergodicity of planar and rough fault simulations may be different.

*Keywords:* Rough faults, Rate-and-state friction, Earthquake cycle simulations,  
Earthquake statistics, Earthquake ruptures, Pulses  
*2010 MSC:* 00-01, 99-00

---

## 1 **1. Introduction**

2 Most modeling studies of earthquakes and the seismic cycle idealize faults as planar  
3 surfaces. However, a large body of work has shown that faults and rock surfaces are not  
4 planar [e.g. 1, 2, 3, 4, 5]. It has been established that fluctuations from planarity in faults  
5 are statistically fractal and self-affine (see Section 1.1 for details). It has become increasingly  
6 important to understand how and when planar models accurately capture key characteristics  
7 of individual ruptures as well as fault behavior during the entire seismic cycles.

8 Recently, several studies have simulated earthquakes on fractal faults. In most cases a  
9 single rupture is simulated, where the stress distribution and initial conditions are assumed  
10 before artificially nucleating the rupture [6, 7, 8, 9]. These studies have included many of  
11 the relevant physics such as off-fault plasticity and full elastodynamic effects. However,  
12 they are too computationally expensive to simulate multiple earthquake cycles which would  
13 include inter-seismic and post-seismic slip, as well as natural nucleation. This means that  
14 the assumed initial stress distribution may strongly influence the length and propagation  
15 characteristics of the simulated ruptures. A more complete approach would ideally allow  
16 stresses to evolve naturally over multiple cycles.

17 Other models have been developed that simulate the whole seismic cycle [10, 11, 12].  
18 However, these methods lack a mechanism for stress dissipation, such as off-fault plasticity,  
19 and are purely elastic. This means that only a few cycles can be simulated before stresses  
20 build-up due to geometric incompatibility and reach unrealistic values. These studies cannot  
21 investigate behavior over multiple cycles. Recently, Allam et al., (2019) [13] used the RSQsim  
22 cycle simulator to simulate seismicity on a self-affine fault over multiple cycles. They used

---

\*Corresponding author:

*Email address:* [ehemiss@caltech.edu](mailto:ehemiss@caltech.edu) (Elías Rafn Heimisson)

23 a backslip to dissipate stresses and thus achieve an efficient way to simulate long term fault  
 24 behavior. However, Allam et al. (2019) used oversized dislocations and did not resolve the  
 25 relevant length-scales that arise from elasticity and the assumed friction law. Such models  
 26 generally produce complex behavior that becomes simpler with grid refinement[14]. Since we  
 27 expect fault roughness to produce complexity, it may be hard to untangle the contribution  
 28 of the oversized dislocations versus the fault roughness.

29 Here I show results from a 2D plane-strain boundary element model with frictional  
 30 properties governed by rate-and-state friction where state evolution evolves according to the  
 31 aging law [15, 16]. The simulations are quasi-dynamic and implement a variation of the  
 32 backslip approach to dissipate stresses. Thus unlike previous work, I report results from  
 33 multiple cycles without unrealistic stress build-up, but at the same time, discretization is  
 34 chosen such that all relevant lengths and time-scales are fully resolved. While many previous  
 35 studies have focused on the amplitude-to-wavelength ratio of the roughness [e.g. 17, 9], I  
 36 focus on systematically varying the minimum roughness wavelength of the fault. The range  
 37 of  $\lambda_{min}$  explored is from 1/3 to 10 times the nucleation length for a planar fault.

### 38 1.1. Background

39 In this study, I investigate a strictly self-similar and statistically fractal fault. Self-  
 40 similarity, in this case, implies the root-mean-square (RMS) fluctuations from planarity  
 41  $h_{RMS}$  are linearly proportional to the fault segment length  $L$  [3], in other words

$$h_{RMS} = \alpha L, \quad (1)$$

42 where  $\alpha$  is the amplitude-to-wavelength ratio. Faults that obey such self-similarity have a  
 43 power spectral density (PSD) [3]:

$$P_h(k) = (2\pi)^3 \alpha^2 |k|^{-3}, \quad (2)$$

44 where  $k = 2\pi/\lambda$  is the wavenumber ( $\lambda$  is the wavelength). Fault roughness is often charac-  
 45 terized in terms of the Hurst exponent  $H$ , where  $h_{RMS} = \alpha L^H$ , with  $H = 1$  implying strict  
 46 self-similarity. Fang and Dunham (2013) [7] showed that for a sufficiently long wavelength

47 slip on a self-similar fault, the average resistance to sliding due to geometric complexity is  
 48 given by the roughness drag:

$$\tau_{drag} = 8\pi^3 \alpha^2 \frac{\mu}{1 - \nu} \frac{\delta}{\lambda_{min}}, \quad (3)$$

49 where  $\delta$  is slip magnitude and  $\lambda_{min}$  is the minimum wavelength that is present in the fault  
 50 profile (other symbols are defined in Table 1). The spatial extent of the slip patch must  
 51 be much larger than  $\lambda_{min}$  for this to be valid. Roughness drag can be generalized to self-  
 52 affine fault [12], but here I focus on the strictly self-similar case. In Section 3.1.1, I will  
 53 use roughness drag to understand the certain rupture characteristic of the simulations in a  
 54 quantitative manner.

55 Typically real faults are found to have  $\alpha$  in the range of  $10^{-3} - 10^{-2}$  [2]. The value  
 56 likely depends on the maturity (cumulative amount of slip) of a fault, which the upper limit  
 57 corresponding to less mature faults [4]. In this study, I have taken  $\alpha = 0.01$ , thus possibly  
 58 representing an immature fault. This choice of  $\alpha$  is also motivated by computational reasons  
 59 since it allows interesting effects of the roughness to manifest at smaller length scales. Some  
 60 studies found fault surfaces to be largely self-affine with a  $H = 0.8$  in the direction of slip,  
 61 but with a different slope at other scales [5]. However, it has been argued that a self-similar  
 62 scaling ( $H = 1$ ) can well fit all resolvable scales simultaneously [8].

63 The roughness drag  $\tau_{drag}$  (Eq. 3) has  $\alpha^2$  dependence on amplitude-to-wavelength ratio,  
 64 for small  $\alpha$  the drag could be assumed small. However, the roughness drag also depends on  
 65  $\delta/\lambda_{min}$ . Implying that  $\tau_{drag}$  diverges as  $\lambda_{min} \rightarrow 0$  for all non-zero values of  $\alpha$ . Clearly if  
 66  $\lambda_{min}$  is sufficiently small, yielding of the material will occur as  $\delta$  increases, thus limiting the  
 67 roughness drag resistance. Fang and Dunham (2013) [7], suggested this may occur when  
 68  $\delta/\lambda_{min} \approx 1$ . The fact that faults are found to be rough over virtually all scales suggests that  
 69  $\lambda_{min}$  may be very small and may, therefore, be an important contributor to  $\tau_{drag}$ , at least  
 70 up to a point when yielding occurs, that is why I have chosen to focus on  $\lambda_{min}$  in this study.

Table 1: Reference parameters that are kept constant in the study

Symbol	Description	Value
<i>Material properties</i>		
$\nu$	Poisson's ratio	0.25
$\mu$	Shear modulus	30 GPa
$c_s$	Shear wave speed	3.5 km/s
<i>Friction</i>		
$d_c$	Characteristic state evolution distance	100 $\mu\text{m}$
$a$	Rate dependence of friction	0.01
$b$	State dependence of friction	0.0125
$V_0$	Steady state sliding velocity	$10^{-9}$ m/s
$f_0$	Steady state coefficient of friction at $V_0$	0.6
$\sigma'_0$	Initial effective normal stress	100 MPa
<i>Fault</i>		
$\alpha$	Amplitude-to-wavelength ratio	0.01
$L$	Fault length along x-axis	10 km
<i>Other parameters dependent on parameters above</i>		
$L_\infty$	Critical crack half-length	$\frac{\mu d_c}{\pi(1-\nu)\sigma_0 b} \cdot \left(\frac{b}{b-a}\right)^2 \approx 29.3825$ m†
$b - a$	Degree of rate-weakening	0.0025
$\eta$	Radiation damping	$\mu/(2c_s) \approx 4.2857$ MPa $\cdot$ s/m † †
$\tau_0$	Initial shear stress	$f_0\sigma_0 + \eta V_0 \approx 60.0000$ MPa
$\theta_0$	Initial state	$d_c/V_0 \cdot (1 + \mathcal{N}(0, 0.01))$
<i>Notes</i>		
†	[18]	
††	[14]	
$\mathcal{N}(m, s)$	Gaussian noise, mean $m$ , std. $s$	

## 71 2. Model Description

72 I use a boundary element method to mesh a fault surface  $h(x)$  (Figure 1). The slip  
 73 on each element (or dislocation) is assumed to be tangential to  $h(x)$  (Figure 1d). That is,  
 74 the dislocation is tilted at an angle  $\theta = \arctan(dh/dx)$ . By use of analytical solutions for  
 75 elastic dislocations in full-space [19] I compute a matrix of influence coefficients that relate  
 76 slip vector  $\boldsymbol{\delta}$  and changes in shear  $\boldsymbol{\tau}$  and normal stress  $\boldsymbol{\sigma}$  at the center of each dislocation:

$$\boldsymbol{\tau}' = \mathbf{G}_\tau \boldsymbol{\delta}' \text{ and } \boldsymbol{\sigma}' = \mathbf{G}_\sigma \boldsymbol{\delta}', \quad (4)$$

77 where the meaning of  $\boldsymbol{\delta}'$  versus  $\boldsymbol{\delta}$  is discussed later. The matrices of influence coefficients are  
 78 compressed using the H-matrix approach of Bradley and Segall (2011) [20]. The frictional  
 79 interface is governed by rate-and-state friction and aging law, respectively:

$$\frac{\tau_0 + \boldsymbol{\tau}' - \eta \mathbf{V}}{\sigma_0 + \boldsymbol{\sigma}'} = f_0 + a \log\left(\frac{\mathbf{V}}{V_0}\right) + b \log\left(\frac{V_0 \boldsymbol{\theta}}{d_c}\right) \quad (5)$$

$$\dot{\boldsymbol{\theta}} = 1 - \frac{\boldsymbol{\theta} \cdot \mathbf{V}}{d_c}, \quad (6)$$

80 where  $\mathbf{V}$  and  $\boldsymbol{\theta}$  represent the slip speed and state at the center of each dislocation respec-  
 81 tively. Eq. 5 can be rearranged to provide an approximation for the slip speed at time step  
 82  $n + 1$  given that the relevant fields are known at time step  $n$ .

$$\mathbf{V}_{n+1} = V_0 \exp\left(\frac{\boldsymbol{\tau}_n - \eta \mathbf{V}_n}{a \boldsymbol{\sigma}_n} - f_0/a - \frac{b}{a} \log(V_0 \boldsymbol{\theta}_n/d_c)\right), \quad (7)$$

83 where  $\boldsymbol{\tau}_n = \tau_0 + \boldsymbol{\tau}'_n$  and  $\boldsymbol{\sigma}_n = \sigma_0 + \boldsymbol{\sigma}'_n$ . It is worth noting that at very high slip speeds ( $\sim$   
 84 1 cm/s) a few iteration are attempted where  $\mathbf{V}_n$  is slightly adjusted to better satisfy Eq. 7,  
 85 otherwise spurious oscillations will appear. The state variable is integrated as

$$\boldsymbol{\theta}_{n+1} = \boldsymbol{\theta}_n + dt_n (1 - \boldsymbol{\theta}_n \mathbf{V}_n/d_c). \quad (8)$$

86 The time step determined by

$$dt_{n+1} = \min([\epsilon d_c / \max(\mathbf{V}_n), \epsilon \min(\boldsymbol{\theta}_n)]), \quad (9)$$

87 where  $\epsilon$  is adjusted such that stability and convergence is found. The slip is updated as at  
 88 each time step:  $\delta_{n+1} = \delta_n + dt_n \mathbf{V}_n$ . The problem is initialized such that  $\boldsymbol{\tau} = \tau_0$ ,  $\boldsymbol{\sigma} = \sigma_0$   
 89 and  $\boldsymbol{\theta} = d_c/V_0(1 + \mathcal{N}(0, 0.01))$  at all dislocation centers (See Table 1). The fault is thus  
 90 approximately at steady state  $\mathbf{V} = V_0$  initially apart from small amplitude Gaussian white  
 91 noise added to the initial state. A planar infinite fault with the same frictional properties  
 92 will oscillate around  $V_0$  as long as the long term average of the elastic stress transfer is  
 93  $\boldsymbol{\tau}' = 0$ . This is reasonable, otherwise the long term average velocity of the fault would be  
 94 changing, which can only occur if the loading is changed. The problem is more complicated  
 95 for a non-planar and/or finite faults if the medium doesn't dissipate the stresses (which is  
 96 the case for a perfectly elastic solid) then as  $\boldsymbol{\delta}$  increases so do the stresses. However, the  
 97 stresses in the medium and on the fault must on average relax at the same rate as the loading  
 98 rate, otherwise they would simply build up indefinitely. I approximate this process using  
 99 the backslip approach [21], where I have defined  $\boldsymbol{\delta}' = \boldsymbol{\delta} - V_0 t$ . Which is then used in Eq.  
 100 4 to compute the elastic stress transfer. This approach differs from the RSQsim backslip  
 101 implementation [21, 13], since I do not have to slip the faults backwards to determine the  
 102 backslip stressing rate. I've simply formulated the problem such that the average steady  
 103 state speed on the fault  $V_0$  is also the loading rate.

104 The fault profile (Figure 1) is stochastically generated with a power spectral density  
 105 in Eq. 2 using the implementation of Dunham et al., (2011) [6]. The dislocation length  
 106 projected on the x-axis was set to 1 m. The smallest  $\lambda_{min} \approx 10$  m and is thus resolved in the  
 107 simulations. Frictional properties (see Table 1) are set such that the crack half-length which  
 108 marks the transition from nucleation to a dynamic instability is constant  $L_\infty \approx 30$  m and is  
 109 therefore also well resolved. The fault profile was generated with  $\lambda_{min}$  ranging from  $L_\infty/3$   
 110 to  $10 \cdot L_\infty$ , but in all cases with the same random seed such that the Fourier decomposition  
 111 at larger wavelengths is identical in both magnitude and phase.

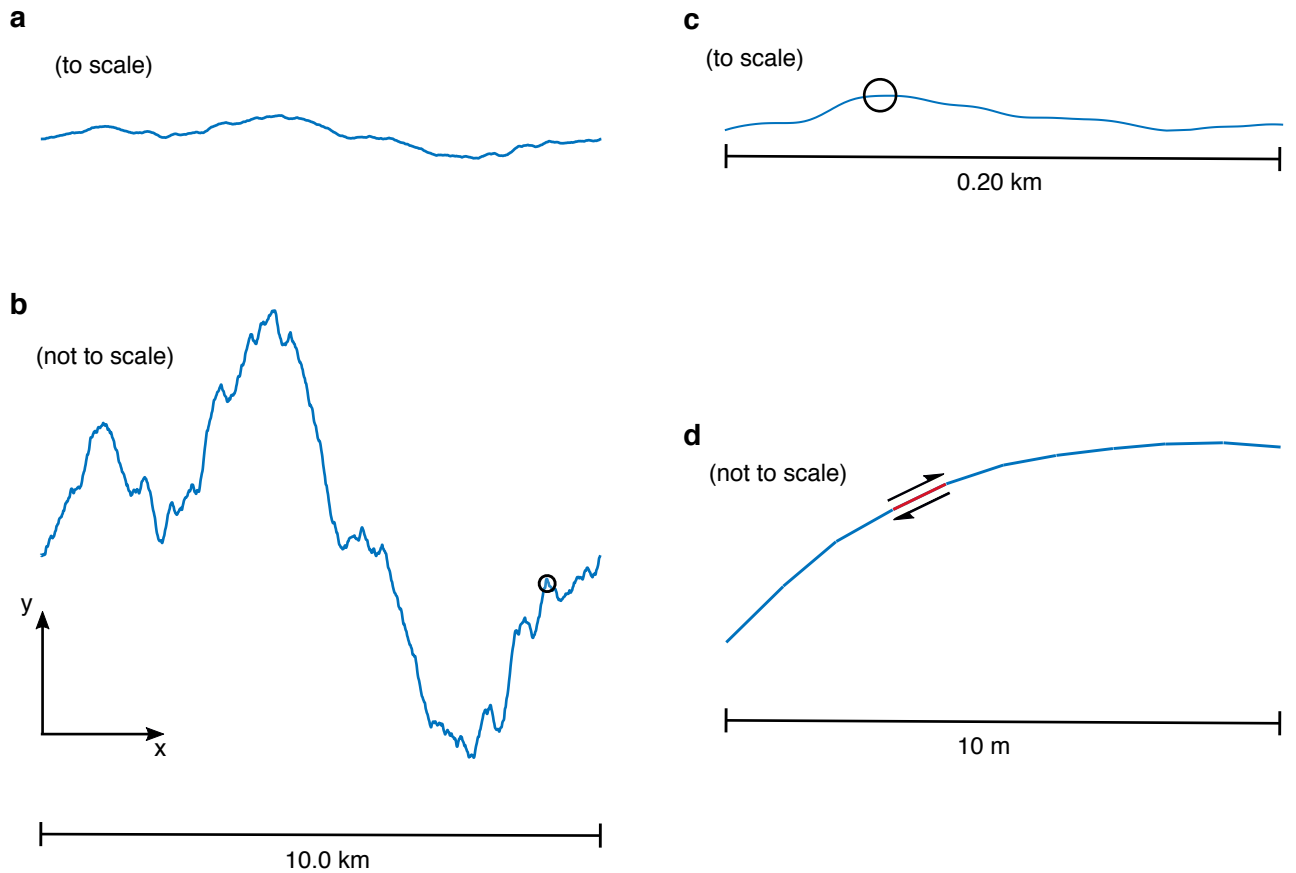


Figure 1: Fault profile at various scales for  $\lambda_{min} = 2L_{\infty}/3$ . **a** shows the entire fault at the correct length to amplitude ratio. **b** same as **a** except with exaggerated amplitude. Small circle shows the location of the fault segment shown in **c**. Circle in **c** shows the fault segment shown in **d** which displays the length scale of the discretization. Red segment shows the length of one dislocation sliding tangentially to the fault topography.

## 112 3. Results

### 113 3.1. Rupture characteristics

114 We start by visualizing the cumulative slip in all simulations (Figures 2, 3 and 4)



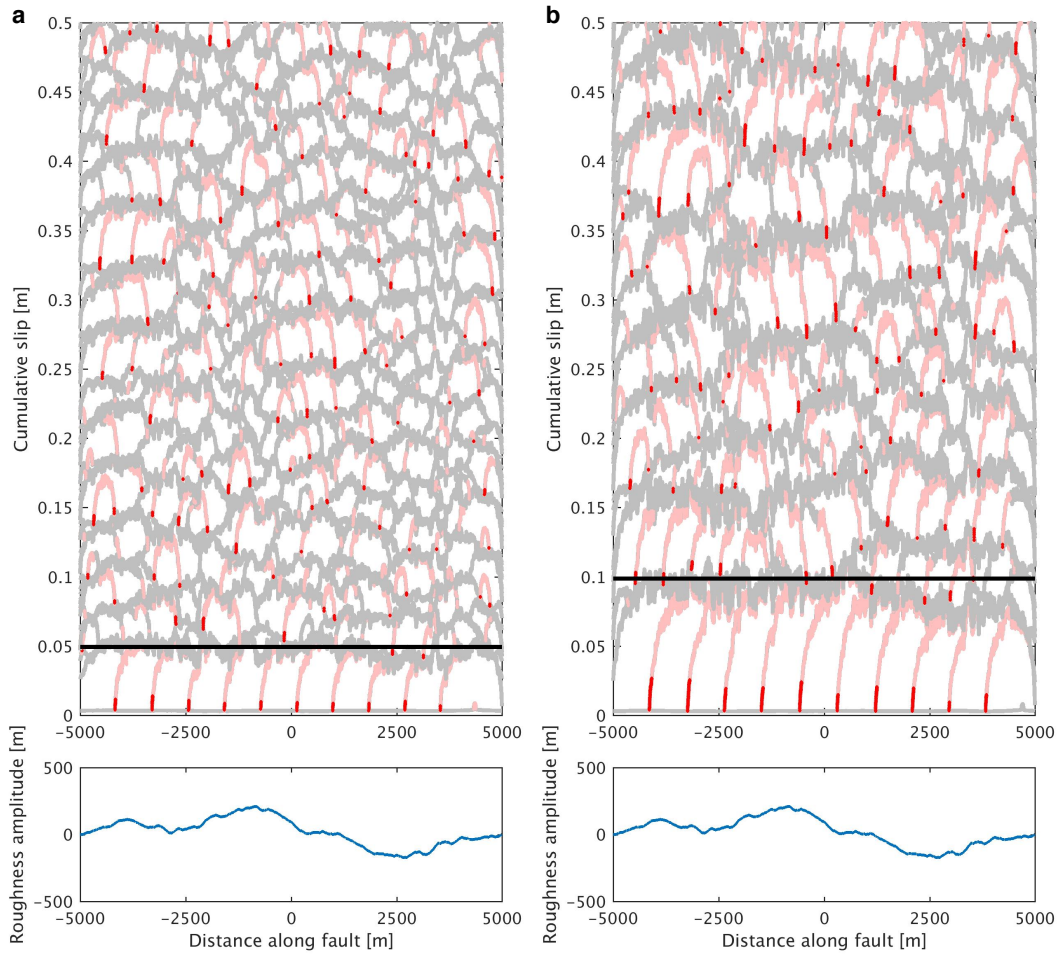


Figure 2: Snapshots of cumulative slip as a function of distance along fault. Red lines indicate points slipping faster than 1 m/s, pale pink lines indicate slip speeds larger than 1 cm/s. Grey lines are points slipping  $\leq 1$  cm/s. **a** shows results for  $\lambda_{min} = L_{\infty}/3$ , **b** shows results for  $\lambda_{min} = 2L_{\infty}/3$ . Bottom panels shows corresponding fault roughness, at the scale shown the fault profiles appear identical. Black line is the estimate of  $\delta_c$ , the maximum slip distance estimate discussed in Section 3.1.1

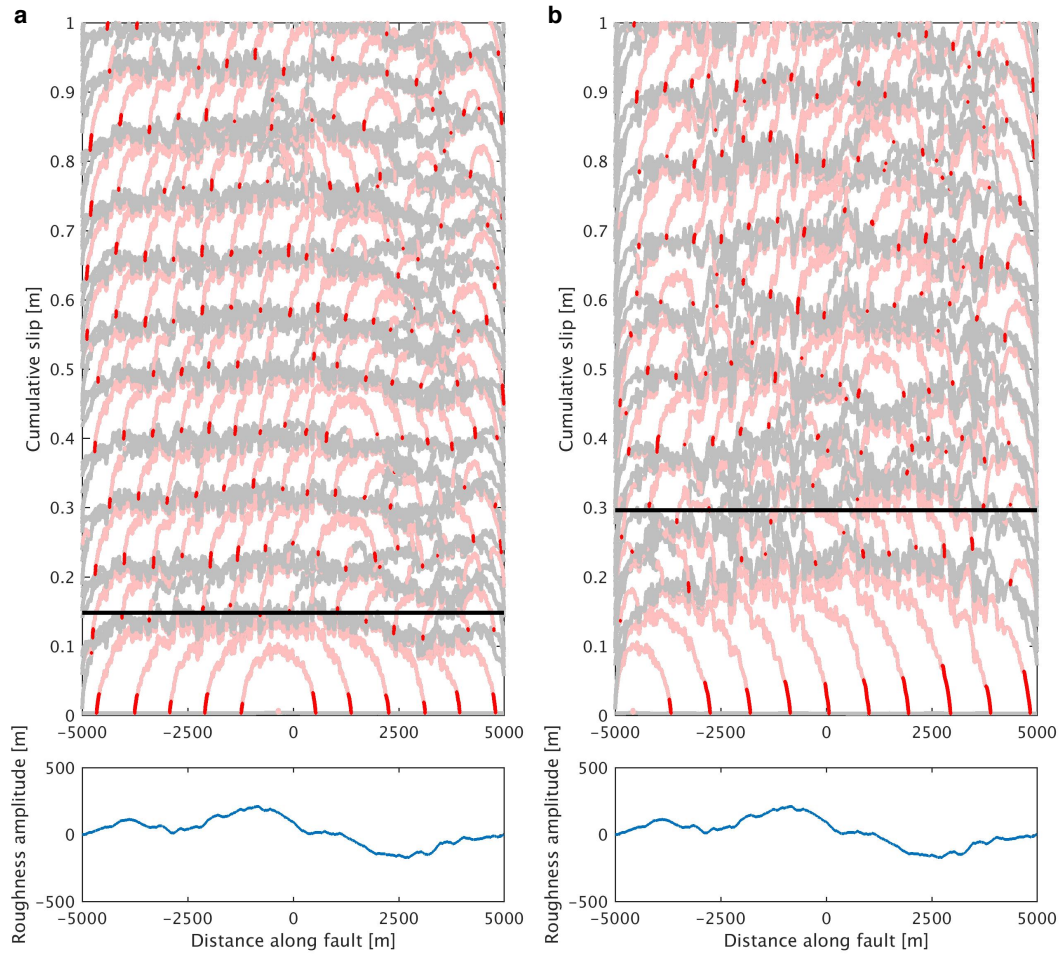


Figure 3: Same as Figure 2 except **a** shows results for  $\lambda_{min} = L_{\infty}$ , **b** shows results for  $\lambda_{min} = 2L_{\infty}$ . Note that the cumulative slip scale is different compared to Figure 2.

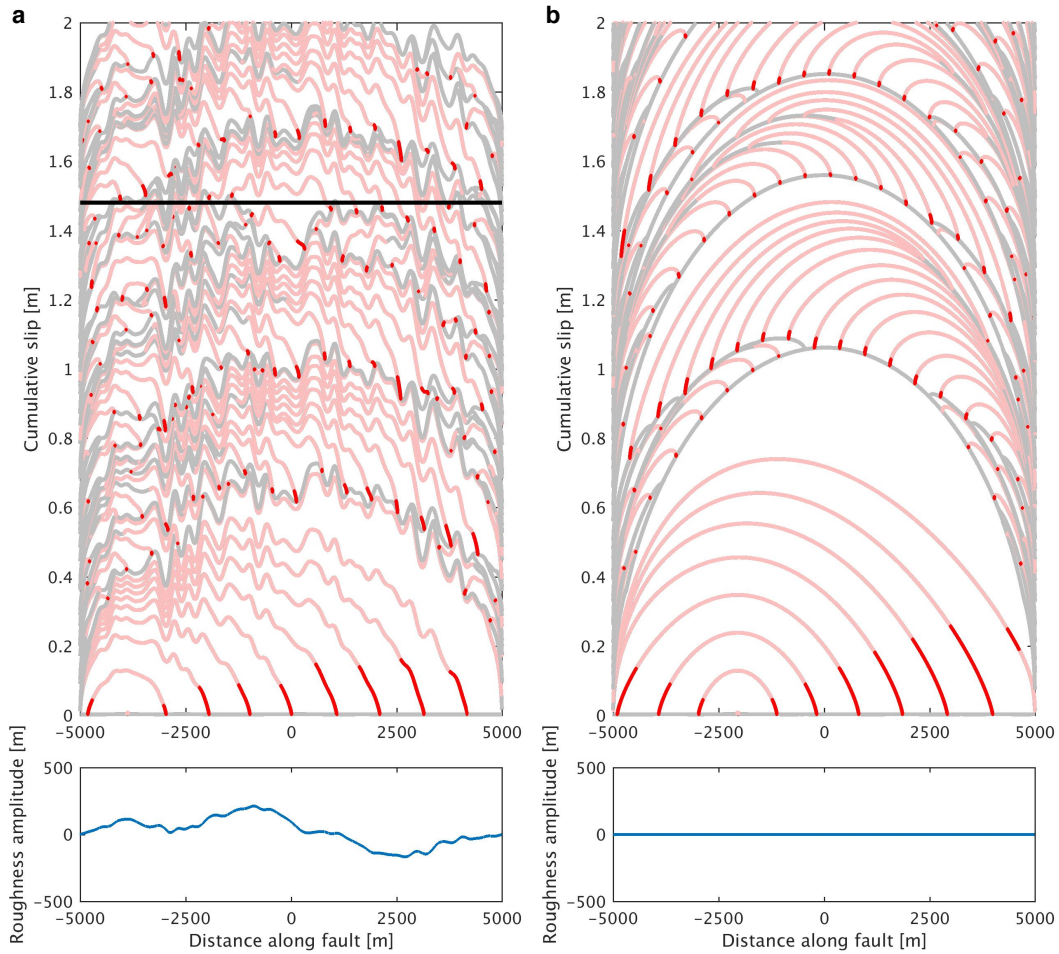


Figure 4: Same as Figure 2 except **a** shows results for  $\lambda_{min} = 10L_{\infty}$ , **b** shows a reference simulation of a planar fault. Note that the cumulative slip scale is different compared to Figures 2 and 3. No  $\delta_c$  value exists for a planar and maximum slip distance is determined by fault finiteness and frictional properties, for **a**  $\delta_c$  significantly over-predicts the maximum slip distance because fault finiteness becomes the limiting factor before slip reaches  $\delta_c$ .

115 From the slip profiles above we observe that initially the rupture always propagates  
 116 the whole length of the fault. However, later events tend to be partial ruptures except  
 117 when  $\lambda_{min}$  is large (Figure 4). Initially, the shear and normal stresses are selected to be  
 118 spatially uniform, and the stress changes due to geometric complexity induced by the ac-  
 119 tively propagating rupture are not sufficient to arrest the rupture. Once the initial rupture

120 has terminated, the resulting heterogeneous stress field can arrest ruptures and limits the  
 121 event sizes. The results thus suggest that the assumed initial stress field in single rupture  
 122 simulations on rough faults may be the primary control on the resulting rupture dimensions.

123 Another important observation from the simulations is that if events become sufficiently  
 124 large, they transition from being crack-like to pulse-like, once they transition to pulse-  
 125 like propagation, the events lock in an approximately fixed amount of slip. This is clear  
 126 in simulations reported in Figures 2 and 3, whereas the fault in Figure 4a isn't sufficiently  
 127 large to show this transition and is qualitatively similar to the planar fault simulation (Figure  
 128 4b). The crack to pulse transition suggests that ruptures may have reached a length scale at  
 129 which roughness drag becomes important (Eq. 3). In the next subsection, I further analyze  
 130 the transition from a crack to pulse.

### 131 *3.1.1. Crack to pulse transition*

132 Let us hypothesize that transition from crack to pulse occurs approximately when the  
 133 stress drop is equal to the roughness drag  $\Delta\tau = \tau_{drag}$ . Under these conditions it cannot be  
 134 energetically favorable for a fault patch to slip further. Assuming a simple constant stress  
 135 drop in-plane crack of half-length  $L_c$  then  $\Delta\tau = (2\mu\bar{\delta})/(\pi(1-\nu)L_c)$ , where  $\bar{\delta}$  is the average  
 136 slip. Setting  $\Delta\tau = \tau_{drag}$  provides:

$$L_c = \frac{\lambda_{min}}{4\pi^4\alpha^2}, \quad (10)$$

137 which we interpret as a characteristic length scale for the crack to pulse transition. Re-  
 138 markably, this scale only depends on roughness parameters  $\lambda_{min}$  and  $\alpha^2$  and not mechanical  
 139 properties of the host rock and not the friction law, as long as the friction law favors in-  
 140 stabilities that become crack-like. By comparing  $L_c$  to slip speed profiles during pulse-like  
 141 propagation, we find that  $L_c$  well characterizes the dimension of the slip patch that is slipping  
 142 approximately fast enough to radiating seismic energy (Figure 5). We may thus consider  $L_c$   
 143 as a characteristic dimension of the pulse. These results suggest that we may estimate  $L_c$   
 144 and therefore  $\lambda_{min}/\alpha^2$  from dynamic slip models that resolve pulse-like propagation ([e.g.  
 145 22]). However, it is worth noting for a 3D rough surface  $L_c$  may be different, at least in

146 terms of prefactor. Further, other mechanisms can result in the manifestation of slip pulses  
 147 on faults, such as low-stress conditions [23], or linear stability at large wavelengths due to  
 148 slip to normal stress coupling [24], which may be responsible for generating the observed  
 149 pulses in nature. It can be shown, although omitted here, that by including roughness drag  
 150 in a linearized stability analysis using rate-and-state friction [e.g. 25], that large wavelengths  
 151 become stable (although not related to normal stress changes). This also gives a length scale  
 152  $\propto \lambda_{min}/\alpha^2$ , albeit with a different prefactor than  $L_c$ .

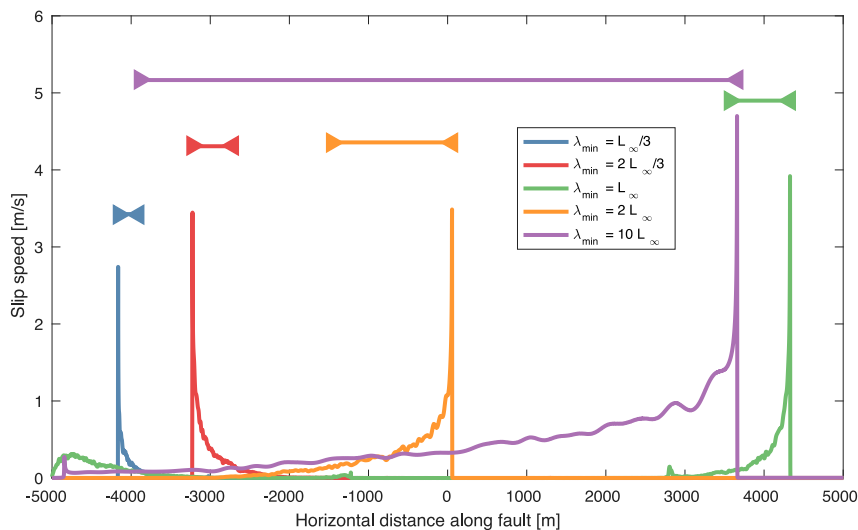


Figure 5: Comparison of  $L_c$  (horizontal lines, Eq. 10) to snapshots of slip speeds during pulse-like propagation during each simulation. The figure suggests that  $L_c$  is a good measure of a characteristic pulse length.

153 We may now use details of the rate-and-state friction law to estimate the maximum  
 154 slip distance during pulse-like propagation. Once pulse reaches a point on the fault, we  
 155 expect that friction rapidly evolves towards steady-state [18]. Locally the stress drop can  
 156 be approximated as  $\Delta\tau_{RS} \approx (b - a)\sigma_0 \log(V_d/V_0)$ , where  $V_d$  could be considered a peak slip  
 157 speed, here we shall take  $V_d = 5$  m/s, thus  $\log(V_d/V_0) \approx 22.3$ . By virtue of the slow growth  
 158 of the logarithm function, a minor error is introduced even if  $V_d$  is an order of magnitude  
 159 smaller (in which case  $\log(V_d/V_0) \approx 20.0$ ). Equating  $\Delta\tau_{RS} = \tau_{drag}$  reveals a maximum slip

160 distance  $\delta_c$  before we expect roughness drag to prevent further slip

$$\delta_c = \lambda_{min} \frac{1 - \nu (b - a) \sigma_0 \log(V_d/V_0)}{\mu 8\pi^3 \alpha^2}, \quad (11)$$

161 which suggests that in a single event,  $\delta \lesssim \delta_c$ . The corresponding values of  $\delta_c$  are plotted as  
162 black horizontal lines in Figures 2, 3 and 4 for each simulation and show excellent agreement  
163 with the slip magnitude in the initial event in all cases where the fault was sufficiently large  
164 to manifest the crack to pulse transition properly. The crack to pulse transition reported  
165 here resembles the changes in the slip distribution of simple static crack calculations done  
166 by Dieterich and Smith (2009) [26] as the crack size was increased. They also reported a  
167 maximum slip distance with the same dependence on  $\lambda_{min}/\alpha^2$  as Eq. 11. However, their  
168 formulation included an unknown fitting coefficient, whereas here no fitting is done.

### 169 *3.2. Seismicity and statistics*

170 As seen in Figures 2, 3 and 4 a single rough or planar fault can host a large distribution  
171 of event sizes. In this section, I investigate the characteristics and statistics of the seismicity  
172 in each simulation, in particular, the seismic moment distribution.

173 To extract discrete events from the simulations some assumptions need to be made about  
174 the dimension and timing of each event. The following criteria are used for identifying a  
175 single event and estimate seismic moment.

- 176 1. Identify a time period where the fault continuously slips at any point faster than 10  
177 cm/s.
- 178 2. Find points where slip during that time was larger than  $d_c$ .
- 179 3. Compute the length of rupture and square to get area.
- 180 4. Compute the average change in slip where slip exceeded  $d_c$ .
- 181 5. Compute the seismic moment and magnitude

182 Clearly squaring the length of a rupture to obtain area is very simplistic and is only  
183 valid if the aspect ratio of the ruptures are constant and other 3D effects, such as those that

184 might arise from event interactions, can be ignored. However, this provides a systematic  
 185 way to compare our in-plane simulations to 3D observations.

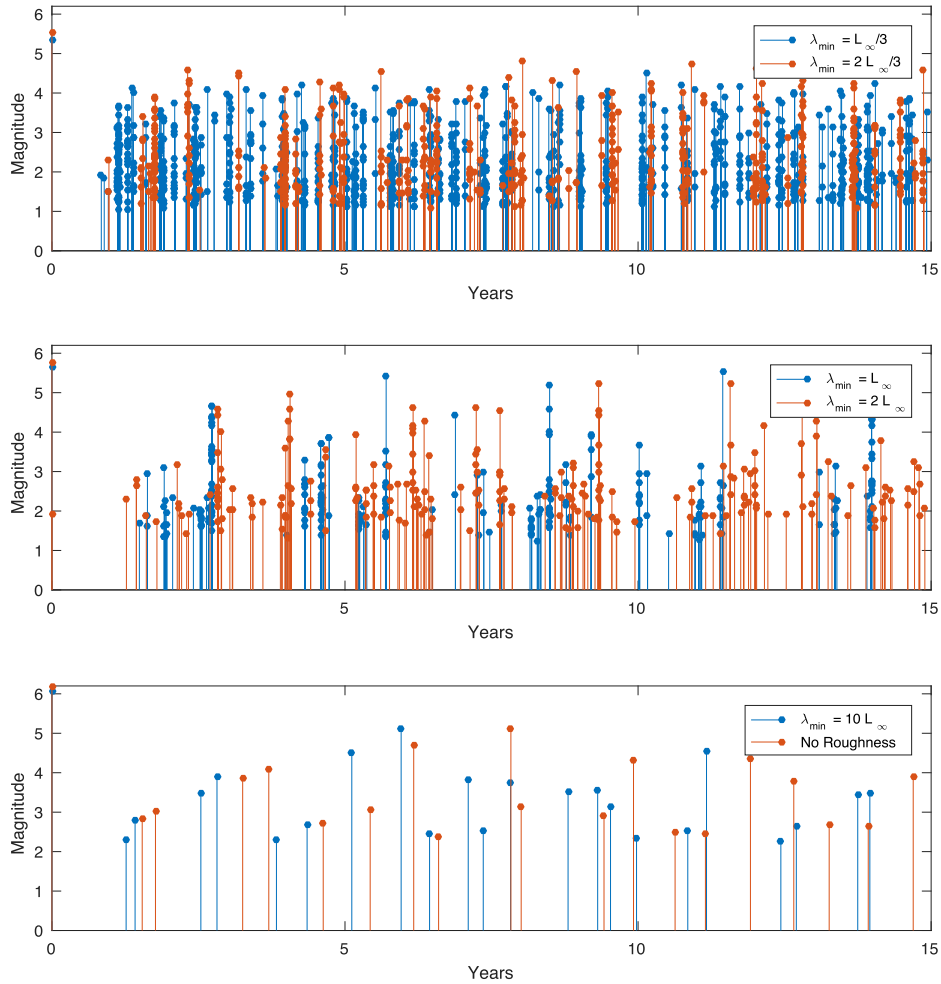


Figure 6: Magnitude versus time in all simulations for the first 15 years of simulations. For small  $\lambda_{min}$ , events are generally smaller and more numerous compared to larger  $\lambda_{min}$  values. Comparison of  $\lambda_{min} = 10L_{\infty}$  and the no-roughness simulation reveals qualitatively similar behavior. The simulations indicated that there is both a maximum and minimum magnitude of events, which change with  $\lambda_{min}$ .

186 Figure 6 reveals very different frequency and magnitudes of seismicity for cases where  
 187  $\lambda_{min}$  is smaller or comparable to  $L_{\infty}$ . If  $\lambda_{min} \gg L_{\infty}$ , the results suggest that the rough fault  
 188 and planar fault are qualitatively similar in terms of the frequency, timing, and magnitudes  
 189 of event. Further, Figure 6 suggests that each simulation has a minimum and maximum

190 moment event. The maximum moment is easy to understand since slip cannot exceed  $\delta_c$   
 191 (Eq. 11), and the fault has a finite length. The minimum moment size is more mysterious  
 192 since by decreasing  $\lambda_{min}$  the minimum moment also decreased. However, by decreasing  $\lambda_{min}$ ,  
 193 the nucleation dimension should increase, which would imply that the smallest event size  
 194 should increase [10]. A possible explanation comes from Eq. 11 where the slip distance is  
 195 reduced, thus limiting the sizes of the events. That explanation is not fully satisfying since  
 196 the smallest events in the simulations tend to arrest before reaching a slip distance of  $\delta_c$ . A  
 197 more likely explanation may be that due to residual stresses, if  $\lambda_{min}$  is decreased, the normal  
 198 stress is locally increased at shorter wavelengths and thus locally the nucleation dimension  
 199 is reduced. This finding highlights the importance of the initial stress in the analysis of  
 200 earthquake nucleation on rough faults.

201 If the simulations presented, have any resemblance to earthquakes in nature, we expect  
 202 that the moment distribution of events to be a power-law. Let us compare the empirical  
 203 probability distribution function (PDF) to a theoretical moment distribution[27]:

$$\text{PDF}(M) = \frac{M_{max}^\beta M_{min}^\beta}{M_{max}^\beta - M_{min}^\beta} \beta M^{-1-\beta}, \text{ where } M_{min} \leq M \leq M_{max}, \quad (12)$$

204 where  $M$  is the moment and  $\beta = 2b/3$ , with  $b$  being the  $b$  value of the Gutenberg-Richter  
 205 distribution, where typically  $b \approx 1$ . For comparison with simulation we have chosen a  
 206 truncated moment distribution since we have inferred from Figure 6 that each simulation  
 207 has both a minimum and maximum moment. Comparison of the theoretical PDF (Eq. 12)  
 208 and the empirical PDF determined from each simulation shows that the two are in generally  
 209 in good agreement for  $b = 0.5$  (Figure 7), which well characterizes the fall-off with increased  
 210 moment. It generally appears  $\lambda_{min}$  does not control the fall-off, but as has been previously  
 211 noted, the truncation of the distribution is changed by  $\lambda_{min}$ . It is notable that even for the  
 212 no-roughness limit, the events follow the same power-law distribution. This is consistent  
 213 with recent work [28], which showed in simulations and theory that a planar fault that is  
 214 sufficiently large could manifest a power-law distribution of events (see further discussion in  
 215 Section 4.1). Some interesting differences are found in Figure 7, when comparing the cases



216 of  $\lambda_{min} \lesssim L_\infty$  to  $\lambda_{min} = 10L_\infty$  and the no-roughness case. We notice that at low values of  
217 moments the empirical distribution has gaps for  $\lambda_{min} = 10L_\infty$  and the no-roughness case,  
218 whereas all gaps for  $\lambda_{min} \lesssim L_\infty$  occur at high moment bins when events are rare. The  
219 latter is most likely due to biased sampling. The synthetic catalog includes approximately  
220 the maximum event size since it is the first event that occurs (Figure 2, 3 and 4), but due  
221 to very numerous small events that increase computational time in these cases, it was not  
222 feasible to simulate long enough sequences that would realize these rare events. However,  
223 for  $\lambda_{min} = 10L_\infty$  and the no-roughness case gaps occur at event sizes that should have been  
224 realized in the catalog. For a larger  $L/L_\infty$  ratio these gaps might disappear. The gaps in the  
225 PDF for a planar fault in Figure 7 are consistent with the bifurcation diagrams by Barbot  
226 (2019)[29], which suggest that certain values of intermediate seismic moments do not occur.  
227 Based on the results in this paper I hypothesize that rough faults may be ergodic in the  
228 sense that if a single simulation is run for long enough events of all possible moments are  
229 realized. However, a planar fault simulation will only realize a subset of the distribution  
230 of possible moments and are thus not ergodic. I conclude that more study of this topic is  
231 needed, in particular in 3D.

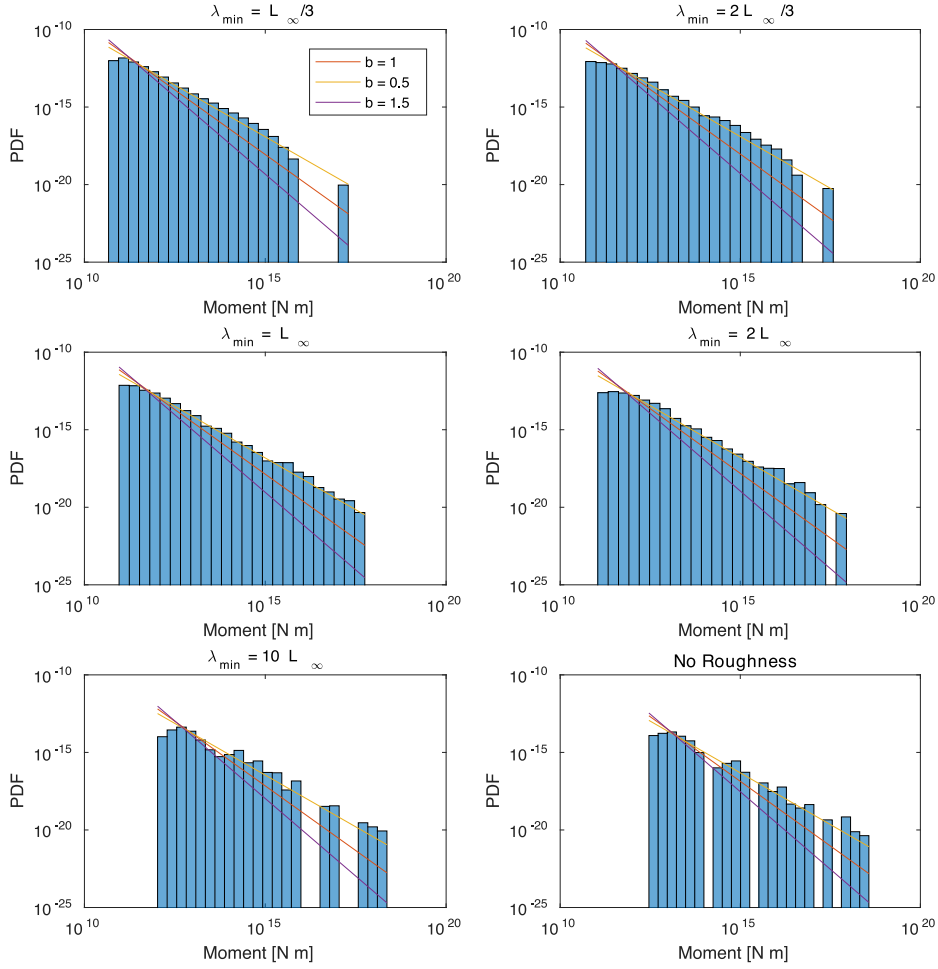


Figure 7: Comparison of Eq. 12 and the empirically estimated moment PDF function. The maximum and minimum moments in Eq. 12 are taken as the observed maximum and minimum moments in the simulations. Eq. 12 is plotted for  $b = 0.5, 1, 1.5$ , the comparison shows that a good agreement between empirical and theoretical PDFs is found for  $b = 0.5$

## 232 4. Discussion

### 233 4.1. The $b$ value

234 The  $b$  value most consistent with the simulations seems to be  $b = 0.5$ , which is consid-  
 235 erably larger than the typically observed value of  $b = 1$  value. The results suggest that the  
 236 value is not related to the roughness since the same value is found for a planar fault, at  
 237 least for  $H = 1$ . Cattania (2019) [28] analyzed an anti-plane fault loaded from below by a

238 creeping velocity strengthening section and bounded from above by a free surface. Through  
239 theoretical considerations of simple crack models, she argued  $b = 3/4$ , which was supported  
240 by simulations. This value is also somewhat larger than typically observed. Cattania (2019)  
241 squared the rupture lengths to attain an area, as was done here. The simplistic treatment  
242 of 3D effect is thus not the source of the difference, although it may factor into what value  
243 of  $b$  is determined from the simulations. The main difference in this study compared to  
244 Cattania (2019) is in the fault loading, here I have simulated a finite in-plane fault that is  
245 loaded using backslip, whereas Cattania (2019) loaded by deep creep and stress build-up at  
246 the top was prevented by a free surface. I suggest that the difference in loading is likely the  
247 cause of the difference in  $b$  value, but I conclude that this issue needs further attention since  
248 it may provide insight into the physical interpretation of  $b$ .

#### 249 *4.2. The backslip approach*

250 The backslip approach to loading and dissipating stresses is a very efficient way of sim-  
251 ulating earthquake cycles for geometrically complex faults. One can argue that stresses on  
252 and off faults in the earth must dissipate on average over multiple cycles at the same rate  
253 as the stresses build-up due to loading. Otherwise, stress accumulation would diverge. The  
254 backslip approach achieves this balance. However, the transient temporal and spatial evo-  
255 lution of the stresses may not be as expected from a more rigorous model that considers  
256 off-fault plasticity using a continuum model of plasticity [e.g. 30, 6, 8]. However, such con-  
257 tinuum plasticity models may not be able to accurately represent an important source of  
258 dissipation that occurs off the main fault on discrete structures such as fault branches [31].  
259 Further developments of earthquake cycle simulations are needed before we can efficiently  
260 simulate multiple cycles on rough faults with realistic stress dissipation mechanisms; in the  
261 meantime, backslip offers a simple way to investigate these problems.

## 262 **5. Conclusions**

263 Roughness has an important influence on both individual ruptures and frequency and  
264 magnitude characteristic of events. Events start as crack-like ruptures, but due to roughness

265 drag, they transition to pulse-like ruptures at a characteristic length-scale determined by  
266 fault roughness alone and not frictional properties or material constants (Eq. 10). Pulses  
267 lock in approximately spatially fixed slip distance (Eq. 11), which depends on the assumed  
268 friction law and material properties. Fault roughness thus offers a plausible mechanism for  
269 earthquakes to transition from cracks to pulses as they grow. I find that decreasing  $\lambda_{min}$ ,  
270 decreases both the maximum and minimum event sizes observed in the cycle simulations,  
271 however, does not appear to alter the inferred  $b$  values which remains the same even for a ref-  
272 erence simulation using a planar fault. Much more numerous small events thus characterize  
273 simulations with small  $\lambda_{min}$  compared to large  $\lambda_{min}$  simulation or planar fault simulations.  
274 The first event in the simulations always ruptures the entire fault, but following events are  
275 generally smaller partial ruptures. This difference suggests that the residual stresses induced  
276 by fault roughness are paramount in determining subsequent events sizes. Caution is needed  
277 when selecting the initial stress distribution for single rupture models on rough faults since  
278 it may significantly influence event sizes. Finally, I've hypothesized that sufficiently rough  
279 faults are ergodic, but planar faults are not, in the sense that a rough fault simulation if run  
280 for long enough will manifest all possible events sizes, but a planar fault will only manifest  
281 a subset of event sizes.

## 282 6. Acknowledgements

283 I want to thank Eric M. Dunham for helpful discussions rough faults. I partially con-  
284 ducted this research while being supported by NASA Headquarters under the NASA Earth  
285 and Space Science Fellowship Program (Grant NNX16AO40H).

## 286 References

- 287 [1] S. R. Brown, C. H. Scholz, Broad bandwidth study of the topography of natural rock surfaces, *Journal*  
288 *of Geophysical Research: Solid Earth* 90 (B14) (1985) 12575–12582. doi:10.1029/JB090iB14p12575.
- 289 [2] W. L. Power, T. E. Tullis, S. R. Brown, G. N. Boitnott, C. H. Scholz, Roughness of natural fault  
290 surfaces, *Geophysical Research Letters* 14 (1) (1987) 29–32. doi:10.1029/GL014i001p00029.
- 291 [3] W. L. Power, T. E. Tullis, Euclidean and fractal models for the description of rock surface roughness,  
292 *Journal of Geophysical Research: Solid Earth* 96 (B1) 415–424. doi:10.1029/90JB02107.

- 293 [4] A. Sagy, E. E. Brodsky, G. J. Axen, Evolution of fault-surface roughness with slip, *Geology* 35 (3)  
294 (2007) 283–286. doi:10.1130/G23235A.1.
- 295 [5] T. Candela, F. Renard, Y. Klinger, K. Mair, J. Schmittbuhl, E. E. Brodsky, Roughness of fault surfaces  
296 over nine decades of length scales, *Journal of Geophysical Research: Solid Earth* 117 (B8). doi:  
297 10.1029/2011JB009041.
- 298 [6] E. M. Dunham, D. Belanger, L. Cong, J. E. Kozdon, Earthquake ruptures with strongly rate-weakening  
299 friction and off-fault plasticity, part 2: Nonplanar faults, *Bulletin of the Seismological Society of Amer-*  
300 *ica* 101 (5) (2011) 2308–2322. doi:10.1785/0120100076.
- 301 [7] Z. Fang, E. M. Dunham, Additional shear resistance from fault roughness and stress levels on geo-  
302 metrically complex faults, *Journal of Geophysical Research: Solid Earth* 118 (7) (2013) 3642–3654.  
303 doi:10.1002/jgrb.50262.
- 304 [8] Z. Shi, S. M. Day, Rupture dynamics and ground motion from 3-d rough-fault simulations, *Journal of*  
305 *Geophysical Research: Solid Earth* 118 (3) (2013) 1122–1141. doi:10.1002/jgrb.50094.
- 306 [9] L. Bruhat, Z. Fang, E. M. Dunham, Rupture complexity and the supershear transition on rough faults,  
307 *Journal of Geophysical Research: Solid Earth* 121 (1) (2016) 210–224. doi:10.1002/2015JB012512.
- 308 [10] Y. Tal, B. H. Hager, J. P. Ampuero, The effects of fault roughness on the earthquake nucleation process,  
309 *Journal of Geophysical Research: Solid Earth* 123 (1) (2018) 437–456. doi:10.1002/2017JB014746.
- 310 [11] Y. Tal, B. H. Hager, Dynamic mortar finite element method for modeling of shear rupture on frictional  
311 rough surfaces, *Computational Mechanics* 61 (6) (2018) 699–716.
- 312 [12] S. W. Ozawa, T. Hatano, N. Kame, Longer migration and spontaneous decay of aseismic slip pulse  
313 caused by fault roughness, *Geophysical Research Letters* 46 (2) (2019) 636–643. doi:10.1029/  
314 2018GL081465.
- 315 [13] A. Allam, K. Kroll, C. Milliner, K. Richards-Dinger, Effects of fault roughness on coseismic slip  
316 and earthquake locations, *Journal of Geophysical Research: Solid Earth* 0 (ja). doi:10.1029/  
317 2018JB016216.
- 318 [14] J. R. Rice, Spatio-temporal complexity of slip on a fault, *Journal of Geophysical Research: Solid Earth*  
319 98 (B6) (1993) 9885–9907. doi:10.1029/93JB00191.
- 320 [15] J. H. Dieterich, Modeling of rock friction: 1. experimental results and constitutive equations, *Journal*  
321 *of Geophysical Research: Solid Earth* 84 (B5) (1979) 2161–2168. doi:10.1029/JB084iB05p02161.
- 322 [16] A. Ruina, Slip instability and state variable friction laws, *Journal of Geophysical Research: Solid Earth*  
323 88 (B12) (1983) 10359–10370. doi:10.1029/JB088iB12p10359.
- 324 [17] Y. Tal, B. H. Hager, The slip behavior and source parameters for spontaneous slip events on rough  
325 faults subjected to slow tectonic loading, *Journal of Geophysical Research: Solid Earth* 123 (2) (2018)  
326 1810–1823. doi:10.1002/2017JB014737.

- 327 [18] A. M. Rubin, J.-P. Ampuero, Earthquake nucleation on (aging) rate and state faults, *Journal of Geo-*  
328 *physical Research: Solid Earth* 110 (B11). doi:10.1029/2005JB003686.
- 329 [19] M. Nikkhoo, T. R. Walter, P. R. Lundgren, P. Prats-Iraola, Compound dislocation models (cdms) for  
330 volcano deformation analyses, *Geophysical Journal International* (2016) ggw427.
- 331 [20] A. Bradley, P. Segall, Efficient numerical modeling of 3d, half-space, slow-slip and quasi-dynamic  
332 earthquake ruptures, in: *AGU Fall Meeting Abstracts*, 2011.
- 333 [21] K. Richards-Dinger, J. H. Dieterich, Rsqsim earthquake simulator, *Seismological Research Letters* 83 (6)  
334 (2012) 983–990.
- 335 [22] J. Galetzka, D. Melgar, J. F. Genrich, J. Geng, S. Owen, E. O. Lindsey, X. Xu, Y. Bock, J.-P. Avouac,  
336 L. B. Adhikari, B. N. Upreti, B. Pratt-Sitaula, T. N. Bhattarai, B. P. Sitaula, A. Moore, K. W. Hudnut,  
337 W. Szeliga, J. Normandeau, M. Fend, M. Flouzat, L. Bollinger, P. Shrestha, B. Koirala, U. Gautam,  
338 M. Bhattarai, R. Gupta, T. Kandel, C. Timsina, S. N. Sapkota, S. Rajaure, N. Maharjan, Slip pulse  
339 and resonance of the kathmandu basin during the 2015 gorkha earthquake, nepal, *Science* 349 (6252)  
340 (2015) 1091–1095. doi:10.1126/science.aac6383.
- 341 [23] G. Zheng, J. R. Rice, Conditions under which velocity-weakening friction allows a self-healing versus a  
342 cracklike mode of rupture, *Bulletin of the Seismological Society of America* 88 (6) (1998) 1466–1483.
- 343 [24] E. R. Heimonsson, E. M. Dunham, M. Almquist, Poroelastic effects destabilize mildly rate-strengthening  
344 friction to generate stable slow slip pulses, *Journal of the Mechanics and Physics of Solids* 130 (2019)  
345 262 – 279. doi:https://doi.org/10.1016/j.jmps.2019.06.007.
- 346 [25] J. R. Rice, N. Lapusta, K. Ranjith, Rate and state dependent friction and the stability of sliding  
347 between elastically deformable solids, *J. Mech. Phys. Solids* 49 (9) (2001) 1865–1898.
- 348 [26] J. H. Dieterich, D. E. Smith, Nonplanar faults: Mechanics of slip and off-fault damage, in: *Me-*  
349 *chanics, structure and evolution of fault zones*, Springer, 2009, pp. 1799–1815. doi:10.1007/  
350 s00024-009-0517-y.
- 351 [27] Y. Y. Kagan, Seismic moment distribution revisited: I. Statistical results, *Geophysical Journal Inter-*  
352 *national* 148 (3) (2002) 520–541. doi:10.1046/j.1365-246x.2002.01594.x.
- 353 [28] C. Cattania, Complex earthquake sequences on simple faults, *Geophysical Research Letters* 0 (0).  
354 doi:10.1029/2019GL083628.
- 355 [29] S. Barbot, Slow-slip, slow earthquakes, period-two cycles, full and partial ruptures, and deterministic  
356 chaos in a single asperity fault, *Tectonophysics* 768 (2019) 228171. doi:https://doi.org/10.1016/  
357 j.tecto.2019.228171.
- 358 [30] E. M. Dunham, D. Belanger, L. Cong, J. E. Kozdon, Earthquake Ruptures with Strongly Rate-  
359 Weakening Friction and Off-Fault Plasticity, Part1: Planar Faults, *Bulletin of the Seismological Society*  
360 *of America* 101 (5) (2011) 2296–2307. doi:10.1785/0120100075.

361 URL <https://doi.org/10.1785/0120100075>

362 [31] X. Ma, A. Elbanna, Dynamic rupture propagation on fault planes with explicit representation of short  
363 branches, *Earth and Planetary Science Letters* 523 (2019) 115702. doi:[https://doi.org/10.1016/  
364 j.epsl.2019.07.005](https://doi.org/10.1016/j.epsl.2019.07.005).